Low-energy electronic structure of the high-T_c cuprates $La_{2-x}Sr_xCuO_4$ studied by angle-resolved photoemission spectroscopy

2007 J. Phys.: Condens. Matter 19 125209

(http://iopscience.iop.org/0953-8984/19/12/125209)

IOP PUBLISHING JOURNAL OF PHYSICS: CONDENSED MATTER

J. Phys.: Condens. Matter **19** (2007) 125209 (23pp) doi:10.1088/0953-8984/19/12/125209

Low-energy electronic structure of the high-T_c cuprates $La_{2-x}Sr_xCuO_4$ studied by angle-resolved photoemission spectroscopy

T Yoshida[1], X J Zhou[2], D H Lu[2], Seiki Komiya[3], Yoichi Ando[3], H Eisaki[4], T Kakeshita[5], S Uchida[6], Z Hussain[7], Z-X Shen[2] and A Fujimori[1]

[1] Department of Complexity Science and Engineering, University of Tokyo, Kashiwa, Chiba 277-8561, Japan
[2] Department of Applied Physics and Stanford Synchrotron Radiation Laboratory, Stanford University, Stanford, CA 94305, USA
[3] Central Research Institute of Electric Power Industry, Komae, Tokyo 201-8511, Japan
[4] National Institute of Advanced Industrial Science and Technology, Tsukuba 305-8568, Japan
[5] Superconductivity Research Laboratory, ISTEC, Shinonome, Koto-ku, Tokyo 135-0062, Japan
[6] Department of Physics, University of Tokyo, Bunkyo-ku, Tokyo 113-0033, Japan
[7] Advanced Light Source, Lawrence Berkeley National Lab, Berkeley, CA 94720, USA

E-mail: teppei@k.u-tokyo.ac.jp

Received 9 August 2006, in final form 16 October 2006
Published 6 March 2007
Online at stacks.iop.org/JPhysCM/19/125209

Abstract

We have performed a systematic angle-resolved photoemission spectroscopy (ARPES) study of the high-T_c cuprates $La_{2-x}Sr_xCuO_4$, ranging from the underdoped insulator to the superconductor to the overdoped metal. We have revealed a systematic doping evolution of the band dispersions and (underlying) Fermi surfaces, pseudogap and quasi-particle features under the influence of strong electron–electron interaction and electron–phonon interaction. The unusual transport and thermodynamic properties are explained by taking into account the pseudogap opening and the Fermi arc formation, due to which the carrier number decreases as the doped hole concentration decreases.

(Some figures in this article are in colour only in the electronic version)

1. Introduction

The mechanism that causes the high-temperature superconductivity in the copper oxide materials (cuprates) is still unknown. As the charge carriers (electrons or holes) are introduced into the parent antiferromagnetic insulator, the material evolves from an insulator to a superconductor, and eventually to a normal metal. Thus, the cuprate systems drastically change their behaviours depending on the carrier density in the two-dimensional CuO_2 planes, which are the stage of the high-T_c superconductivity and related low-energy physics. While the overdoped ($x > 0.2$) cuprates behave like a relatively conventional Fermi liquid above T_c,

underdoped ($x < 0.15$) cuprates in the normal state show behaviours which are strongly deviated from those of a standard Fermi liquid. Therefore, it is necessary to know the detailed information about the doping evolution of the electronic structure of the CuO_2 plane to understand the cuprate systems.

The recent remarkable development in the angle-resolved photoemission spectroscopy (ARPES) technique has enabled us to investigate fine spectral features near the chemical potential, which may be used to interpret the thermodynamic and transport properties of solids from a microscopic point of view. Indeed, ARPES studies on cuprate superconductors, largely on the $Bi_2Sr_2CaCu_2O_{8+y}$ (Bi2212) family, have been performed extensively [1] and revealed the normal-state electronic structure such as the dispersions of quasi-particle bands crossing the chemical potential, the presence of a pseudo-gap above T_c and its d-wave-like gap anisotropy in the underdoped region. On the other hand, bilayer splitting [2], BiO-layer structural modulation, etc complicate the interpretation of the ARPES spectra of Bi2212.

In order to avoid the above complications and to study the intrinsic doping dependence of the electronic structure over a much wider hole concentration range, the $La_{2-x}Sr_xCuO_4$ (LSCO) system is the most suitable one among the families of high-T_c cuprate superconductors. LSCO has a simple crystal structure with single CuO_2 layers, and no Cu–O chains as in $YBa_2Cu_3O_{7-y}$ (YBCO) nor complicated structural modulation of the block layers as in Bi2212. The hole concentration in the CuO_2 plane can be controlled over a wide range and uniquely determined by the Sr concentration x (and the small oxygen non-stoichiometry). One can therefore investigate the doping dependence from the undoped insulator ($x = 0$) to the heavily overdoped metal ($x = 0.3$) in a single system. Indeed, the most extensive set of data on the doping dependence of the transport and thermodynamic properties are available for the LSCO system [3–9] and can be in principle compared with ARPES data.

ARPES studies of LSCO had been behind those of Bi2212 for some time due to the experimental difficulties in obtaining atomically flat surfaces by cleaving and to the relatively poor surface chemical stability. The first successful ARPES study of LSCO was performed by Ino *et al* [10]. They showed an overall feature of band dispersions and Fermi surface, including a crossover from a hole-like to an electron-like Fermi surface with hole doping [10–12]. Peculiar features such as an unusual suppression of the zone diagonal direction, which had not been observed in Bi2212, were also reported in [10] and subsequently by Zhou *et al* [13]. In addition, so-called 'two-component' behaviour, namely, the coexisting remnant lower Hubbard band and quasi-particle band with the chemical potential pinned within the charge-transfer gap, have been observed in the underdoped region [11]. These unconventional behaviours were discussed in terms of microscopic charge inhomogeneity or the spin-charge fluctuations in a stripe form [14, 15], which has been suggested from incommensurate peaks in the inelastic neutron scattering studies [16]. Alternatively, the apparent 'two-component' behaviours in the ARPES line shapes have been interpreted by the strong electron–phonon coupling [17–19].

Because of the weakness of the nodal spectral weight, concerns about the sample surface quality had persisted. Also, there were questions about the effects of photoemission matrix elements [20], which makes it difficult to extract quantitative information about the stripe effects from comparison between experiment and theoretical studies which predicted the suppression of spectral weight in the nodal direction [21–24]. However, recent ARPES studies on LSCO have revealed that under a suitable experimental geometry, a quasi-particle (QP) band with a clear kink feature crosses the Fermi level (E_F) in the nodal (0, 0)–(π, π) direction [25] even down to the lightly doped region [26]. It has also been established that the Fermi surface is basically large [27] and that the (π, 0) region remains (pseudo-) gapped, leading to the electronic state in which only part of the Fermi surface survives as an 'arc' around the nodal direction. Such a large Fermi surface picture with the pseudogap has been theoretically studied

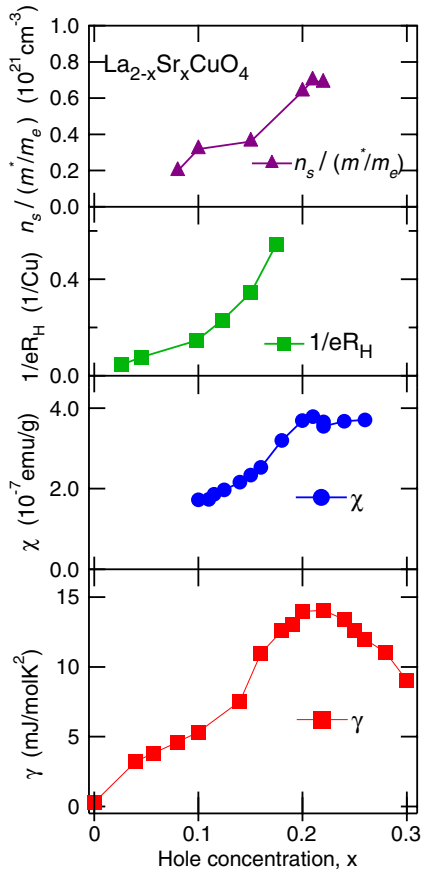

Figure 1. Doping dependence of the electronic specific coefficient γ [9], Pauli paramagnetic susceptibility χ [3], the carrier density deduced from Hall coefficient R_H [31], and the superfluid density n_s/m^* [32] in LSCO.

both from RVB [28] and Fermi liquid approaches [29]. In this paper, we present a large set of ARPES spectra of LSCO showing the QP structure or the pseudogap feature on the entire Fermi surface, and compare the ARPES spectra with the transport and thermodynamic properties in the entire doping range. Particularly, we demonstrate that, in the underdoped region, both the ARPES spectra and the physical properties are highly affected by the opening of the pseudogap and the concomitant formation of the Fermi arc.

Figure 1 summarizes the pseudogap behaviours seen in the thermodynamic and transport properties of LSCO. As shown in the figure, the electronic specific coefficient γ [9] and the Pauli paramagnetic susceptibility χ [3] decrease with decreasing x, in contrast to the mass enhancement toward the metal–insulator transition usually considered in the Fermi-liquid picture and experimentally seen in the Fermi-liquid system $La_{1-x}Sr_xTiO_3$ [30]. Furthermore, although the Fermi surface seen by ARPES is large, the carrier density n deduced from the Hall coefficient R_H [31] and the superfluid density n_s from magnetic-field penetration depth [32] measurements decrease with decreasing x. That is, the carrier number n appears to be given by the hole concentration x rather than the band filling $1 - x$ in the underdoped region [31, 33]. These unconventional behaviours may be attributed to the pseudogap opening through which a portion of the Fermi surface becomes gapped above T_c. The pseudogap opening provides a

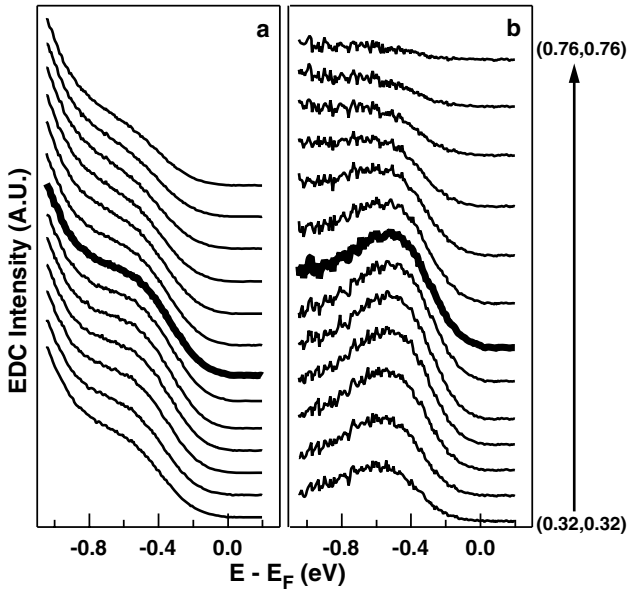

Figure 2. Photoemission spectra of La_2CuO_4 along the (0, 0)–(π, π) nodal direction in the first Brillouin zone [18]. The corresponding momentum runs from $(0.32, 0.32)\pi$ to $(0.76, 0.76)\pi$, as indicated by the arrow. (a) Raw data. (b) To highlight the momentum dependence, a 'background' given by a spectrum near (π, π) has been subtracted. In both (a) and (b), the bold curves correspond to a momentum closest to $(\pi/2, \pi/2)$.

natural scenario to the long-standing issue of how the electronic structure evolves with hole doping from the Mott insulator to the superconductor in two-dimensional systems. These features will be described by the recent high-quality ARPES data of LSCO as described below.

2. Experiment

The ARPES measurements were carried out at beamline 10.0.01 of the Advanced Light Source (ALS) and beamline 5-4 of Stanford Synchrotron Radiation Laboratory (SSRL), using incident photons with energies of 55.5 and 22.4 eV, respectively. SCIENTA SES-2002 (ALS) and SES-200 (SSRL) spectrometers were used in the angle mode. The total energy resolutions were about 15 meV (SSRL) to 20 meV (ALS). High-quality single crystals of LSCO were grown by the travelling-solvent floating-zone method. The samples were cleaved *in situ* and measurements were performed at about 20 K (ALS) or 10 K (SSRL). In the measurements at ALS, the electric field vector **E** of the incident photons lies in the CuO_2 plane, rotated by 45° from the Cu–O bond direction, so that its direction is parallel to the Fermi surface segment around the nodal region. This measurement geometry enhances dipole matrix elements in this **k** region [25].

3. Doping evolution of the electronic structure

3.1. Doping evolution of quasi-particles

One of the central issues in the field of high T_c cuprates is how an antiferromagnetic insulator evolves with hole doping. Figure 2 reveals some important features such as the doping-

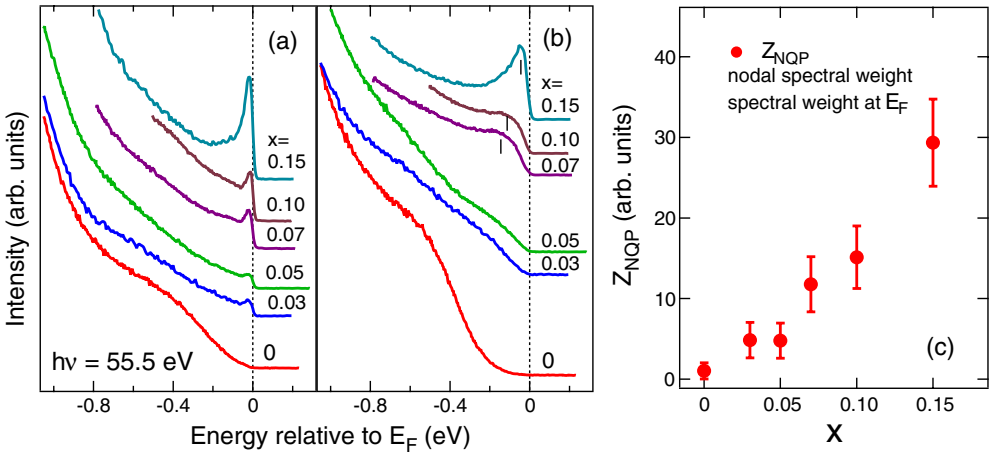

Figure 3. ARPES spectra at $\mathbf{k} = \mathbf{k}_F$ in the nodal direction in the second Brillouin zone (BZ) (a) and those at $(\pi, 0)$ (b) for various doping levels [26]. (c) Doping dependence of the nodal QP spectral weight, Z_{NQP}.

dependent dispersions along the (remnant) Fermi surface and spectral weight transfer from the high-energy Hubbard band to the low-energy QP band. In order to further look into this problem, first, we show the energy distribution curves (EDCs) of the lowest energy feature along the nodal direction of undoped La_2CuO_4. One can see one broad dispersive feature approximately folded back with respect to the $(\pi/2, \pi/2)$ point [18], similar to the results for $Ca_2CuO_2Cl_2$ [17]. As in the case of $Sr_2CuO_2Cl_2$, the dispersion of this feature agrees with that of the t–t'–t''–J model well [34–36]. The broad band at ∼0.5 eV has been interpreted as a boson side band showing a Franck–Condon broadening. A shell-model calculation showed that the width of the phonon sideband is in good agreement with the ARPES data of undoped La_2CuO_4 [18]. This indicates that the electron–phonon coupling is strong enough, which seems a universal feature in the undoped cuprates.

Next, let us look at the doping evolution of the spectral intensity of the QP in LSCO. Figures 3(a) and (b) show the evolution of spectra at $\mathbf{k} \sim (\pi/2, \pi/2)$ and $(\pi, 0)$, respectively, with hole doping [26]. At $\sim(\pi/2, \pi/2)$, a finite spectral weight exists at E_F except for $x = 0$, and increases with x without an abrupt change across the 'insulator'–superconductor transition boundary of $x \sim 0.06$. Note that, even in the lightly doped non-superconducting $x = 0.03$, a QP peak is depressed and crosses the chemical potential in the nodal direction and forms a Fermi 'arc'. This would explain the metallic behaviour at high temperatures of the lightly doped materials [37]. To see the doping evolution of QP, the spectral weight is plotted in figure 3(c) as a function of hole doping x. Here, the nodal QP weight Z_{NQP} is defined as the peak intensity of the EDC at k_F in figure 3(a). In the underdoped regime, Z_{NQP} increases rapidly with hole doping, exhibiting an apparent similarity to the doping evolution of the Drude weight in the optical conductivity [33]. The observed finite spectral weight at $x = 0.03$ is consistent with the optical study of lightly doped LSCO, which has shown that the Drude weight is finite already in $x = 0.03$ [38].

3.2. Fermi surface and two-dimensional band structure

In order to deduce the Fermi surface or 'underlying' Fermi surface, we have performed spectral-weight mapping at the chemical potential in the momentum space for various doping levels as

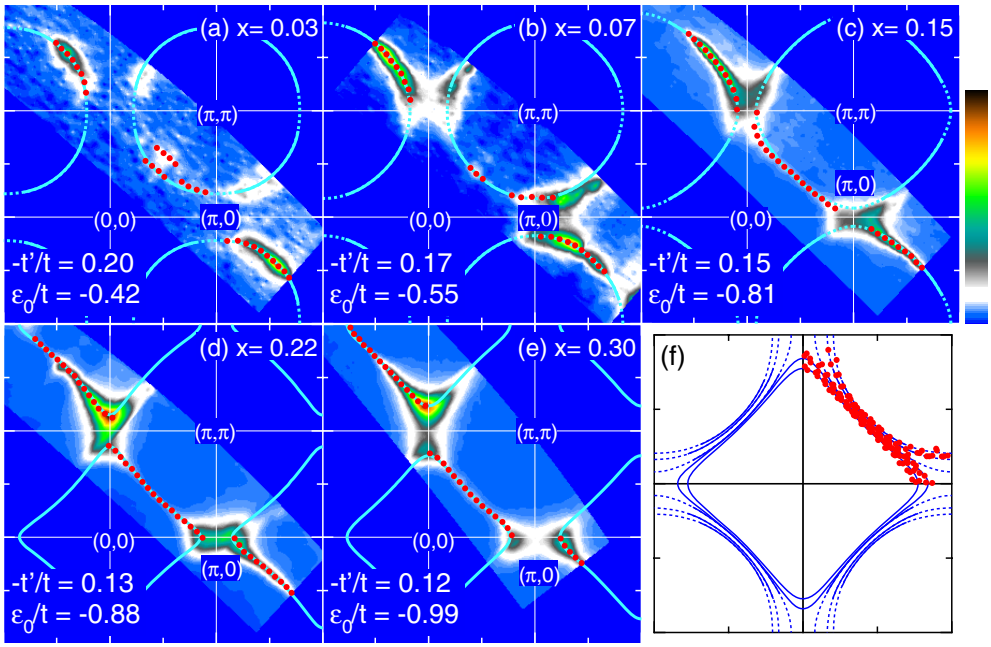

Figure 4. Spectral weight mapping in k-space at the chemical potential in LSCO. Data were taken with $h\nu = 55.5$ eV. The dots indicate k_F positions determined by the peaks of momentum distribution curves (MDCs) at the chemical potential. The curves show the Fermi surface interpolated using the tight-binding model [27]. The evolution of the Fermi surface with doping is more clearly seen in panel (f).

shown in figure 4 [27]. The spectral-weight distribution of the overdoped $x = 0.3$ as well as $x = 0.22$ samples clearly shows an electron-like Fermi surface [25]. Spectral weight near $(\pi, 0)$, a remnant $(\pi, 0)$ feature of the flat band [25], becomes weaker in going from $x = 0.22$ to 0.30, indicating that the more heavily the samples are overdoped, the more the electronic structure becomes conventional Fermi-liquid-like. The Fermi surface topology changes from electron-like in $x = 0.22$ to hole-like in $x = 0.15$, which may cause an electronic topological transition (ETT) [39]. Below $x = 0.15$, the nodal direction in the second Brillouin zone (BZ) becomes more intense than that around $(\pi, 0)$, in contrast to $x = 0.22$ and 0.3, due to the superconducting or pseudogap opening with d-wave symmetry in the underdoped and optimally doped regions. In the lightly doped $x = 0.03$ (panel (a)), the $(\pi, 0)$ spectral weight almost disappears, and only the spectral weight around the zone diagonal direction remains appreciable around the chemical potential.

The EDCs along the $(0, 0)$–$(\pi, 0)$–(π, π) lines for various doping levels are shown in figure 5 and their intensities along the same lines are plotted in the energy–momentum E–k space in figure 6. One can see that the flat band feature appears around $(\pi, 0)$ in the optimally and underdoped region $x \leqslant 0.15$, while the QP dispersion crosses the chemical potential along the $(0, 0)$–(π, π) line. Also, the intensity plots clearly show how the intensity at the chemical potential around $(\pi, 0)$ becomes weak for $x \leqslant 0.15$ as the pseudo-gap and/or the superconducting gap opens around $(\pi, 0)$. One can see from figure 5 that the line width around $(\pi, 0)$ becomes broad with decreasing x, indicating increasing antiferromagnetic correlation with decreasing x. Also, the 'two-component' behaviour is clearly seen in the EDCs of the lightly doped samples with $x = 0.03$ and 0.05.

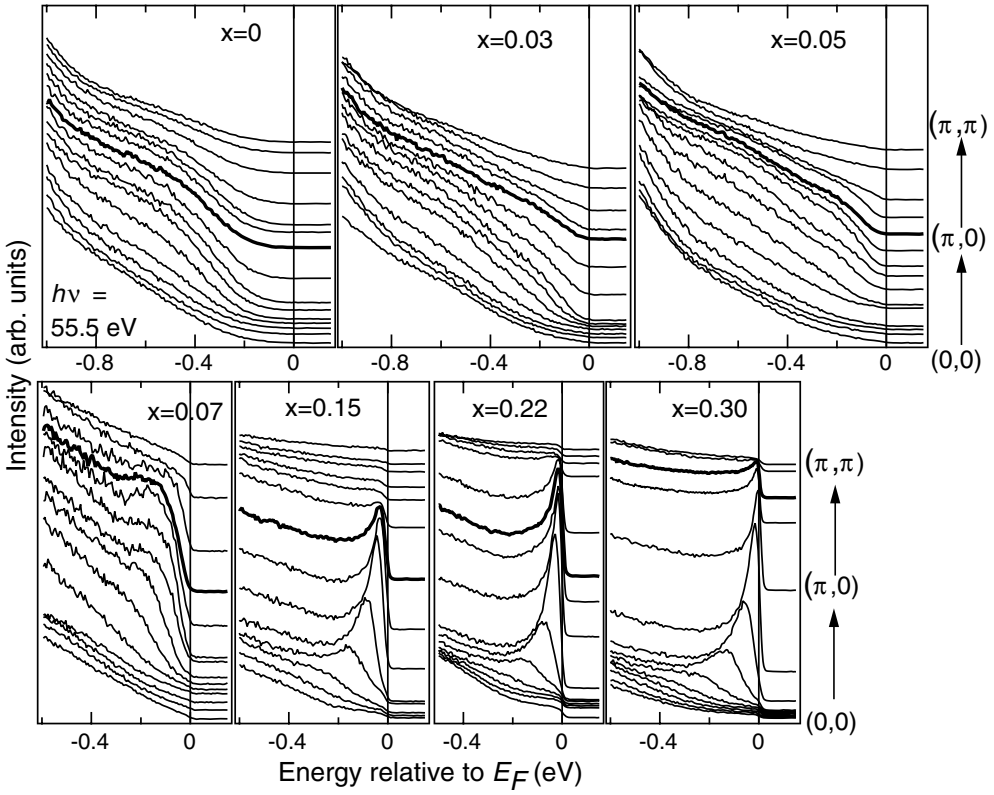

Figure 5. Energy distribution curves (EDCs) along the (0, 0)–(π, 0)–(π, π) lines for various doping levels in LSCO. Thick curves represent the spectra at (π, 0). The spectra along the (0, 0)–(π,0) line are from the second BZ.

The 'two-component' behaviour in LSCO [11, 26] was interpreted in terms of microscopic charge inhomogeneity or stripe. According to a recent theoretical study, a mixed phase of antiferromagnetic and superconducting states has been proposed to explain the characteristic 'two-component' behaviour in LSCO [40]. At the same time, a new way to interpret the 'two-component' spectral feature in terms of polaronic effects has also emerged [17, 19, 18]. In the new picture, the high energy ∼0.5 eV has been interpreted as polaronic side bands. These two interpretations may be related to each other because it has been predicted that phase separation between the insulating and metallic phases occurs under a certain regime of electron–phonon coupling strengths [41].

The Fermi surfaces obtained from the two-dimensional tight-binding fits are superimposed on the spectral weight mapping in figure 4. The experimental k_F values have been fitted to the two-dimensional (2D) single-band tight-binding (TB) model

$$\varepsilon_k = -2t[\cos(k_x a) + \cos(k_y a)] - 4t' \cos(k_x a)\cos(k_y a) - 2t''[\cos(2k_x a) + \cos(2k_y a)] + \varepsilon_0, \quad (1)$$

as shown by blue curves. Here, t, t' and t'' are the first, second and third nearest neighbour transfer integrals between Cu sites. We have assumed constant $t = 0.25$ eV and relationship $-t''/t' = 1/2$ for all the doping levels, and regarded t' and ε_0 as adjustable parameters. The Fermi surface could be well fitted by the TB model, although some misfit can be seen for the

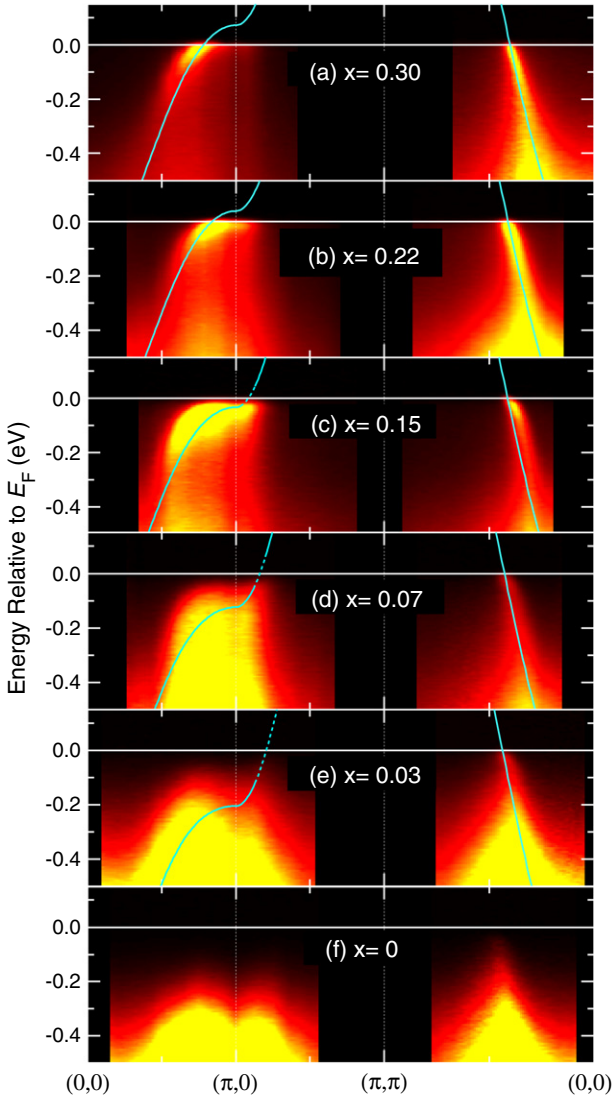

Figure 6. Intensity plot in E–k space along the symmetry lines (0, 0)–(π, 0)–(π, π)–(0, 0) in LSCO. Data were taken with $h\nu = 55.5$ eV. The curves show the tight-binding band dispersion with the parameters shown in figure 4.

kink structure, which arises from coupling to phonons as discussed in section 4 [42, 43] and the extremely flat band dispersion around (π,0) in the underdoped region as shown in figure 6. In figure 4(f), the deduced Fermi surfaces for various x values are replotted, clearly showing the change of the Fermi surface shape and topology with x. The TB dispersions with the same parameters are superimposed on the colour mapping in figure 6. Overall features of the Fermi surfaces and band dispersions are in good accordance with the results of the local-density-approximation (LDA) band-structure calculations [44].

The obtained TB parameters $-t'/t$ shown in figure 4 exhibit a clear doping dependence. The increase of $-t'/t$ with decreasing x can be qualitatively explained by the increase of the Cu–apical oxygen distance with decreasing x [45]. In figure 7(a), the $-t'/t$ values are plotted

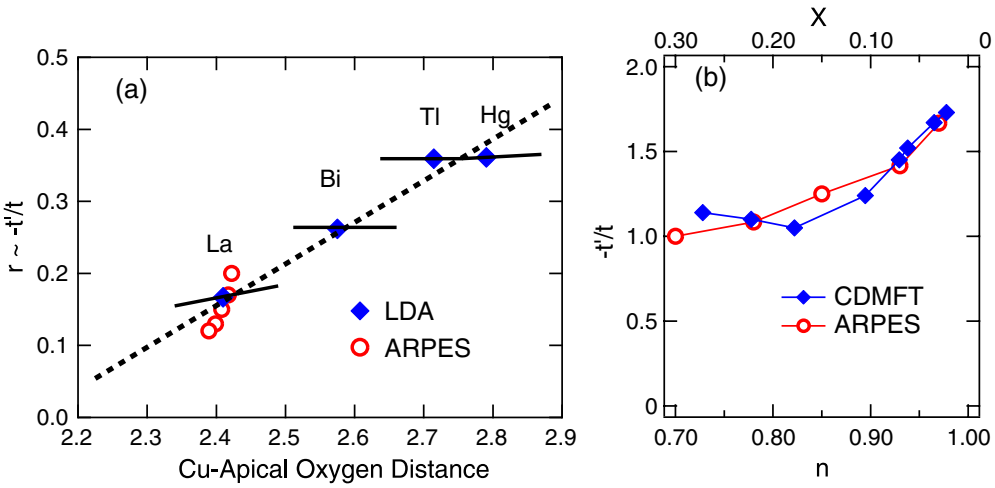

Figure 7. Comparison of the $-t'/t$ values deduced from the tight-binding fit to the ARPES data with theoretical predictions. (a) Comparison between $-t'/t$ calculated by LDA [46] (filled diamond) and those estimated from ARPES (circle), plotted as a function of the Cu–apical oxygen distance [45]. The largest and smallest $-t'/t$ in the ARPES data corresponds to those of $x = 0.03$ and 0.30 samples, respectively. (b) Comparison of t'/t estimated from the ARPES Fermi surface and those calculated using CDMFT [47]. The theoretical values have been normalized to the bare (i.e. input) t'/t, while the experimental values have been normalized to the values at $x = 0.3$. $n = 1 - x$ is the electron number.

as a function of the Cu–apical oxygen distance [45] and compared with those of the LDA calculation by Pavarini *et al* [46]. The obtained $-t'/t$ agree rather well with the results of the LDA calculations $-t'/t \sim 0.15$ [46]. The LDA calculation has indicated that the larger Cu–apical oxygen causes the larger $-t'/t$, which is consistent with the trend in the obtained $-t'/t$ values deduced here. The present result is also consistent with the cellular dynamical mean field theory (CDMFT) calculation [47], in which the momentum dependence of the self-energy has been taken into account by using a cluster instead of a single impurity atom in DMFT. As shown in figure 7(b), the CDMFT calculation has indicated that increasing correlation effects in the underdoped region are reflected in the effective increase of the $-t'/t$ value. It therefore seems that both the structural effects as predicted by the LDA calculation and the correlation effects as predicted by the CDMFT calculation increase $-t'/t$ as x decreases and explain the ARPES results.

As for Luttinger's sum rule, the underlying 'Fermi surface' of LSCO determined from the low energy spectral weight of ARPES approximately fulfils it remarkably well even down to the lightly doped region as shown in figure 8(a) [27]. This is in strong contrast with the results on Na-CCOC, which shows a clear deviation from Luttinger's sum rule in the underdoped region [48]. These differences between LSCO and Na-CCOC may be related to the difference in the t'/t value and/or to the difference in the electron–lattice coupling strength. In relation to the area of the Fermi surface, the shape of the Fermi surface may be characterized by the position of the Fermi surface along the nodal direction. As shown in figure 8(b), the same position in Na-CCOC shows a strong doping dependence and is extrapolated to $(\pi/2, \pi/2)$ in the $x = 0$ limit, whereas in LSCO the limiting value is off the $(\pi/2, \pi/2)$ point [27]. This may be related to the observation that the chemical potential approaches the top of the lower Hubbard band in Na-CCOC as the doping decreases, whereas the chemical potential stays away from the lower Hubbard band in LSCO [49, 17, 50].

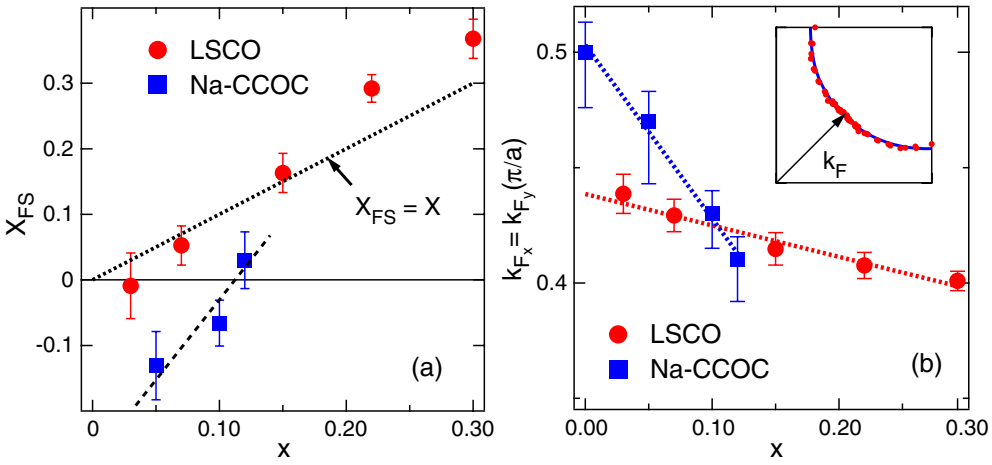

Figure 8. Fermi surface area and shape of LSCO as functions of doping [27]. Data for Na-CCOC [48] are also plotted. (a) Doping dependence of the hole number x_{FS} deduced from the Fermi surface area. Luttinger's sum rule $x_{FS} = x$ is shown for comparison. (b) Fermi surface position in the nodal direction.

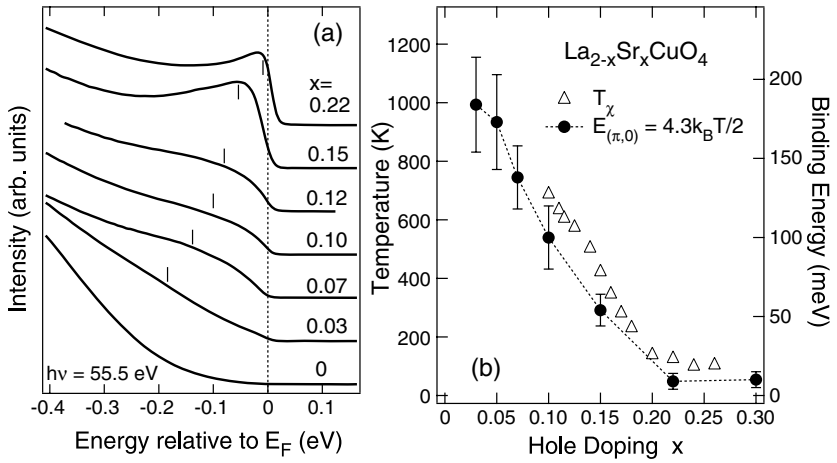

Figure 9. Angle-integrated photoemission spectra and the large pseudogap. (a) Spectrum for each doping. Vertical bars represent the binding energy of the flat band. (b) The doping dependence of the binding energy of the flat band is compared with the characteristic temperature T_χ where the magnetic susceptibility $\chi(T)$ takes a maximum [3].

3.3. Large pseudogap and small pseudogap

There are two kinds of 'pseudogaps' in the high-T_c cuprates, called a 'small pseudogap' and a 'large pseudogap'. First, we discuss the relationship between the high-energy pseudogap behaviours, which have been observed as a characteristic temperature in the magnetic susceptibility $\chi(T)$ [3] and the Hall coefficient $R_H(T)$ [4], and a characteristic energy in the photoemission spectra. As shown in figure 9(b), the doping dependence of the flat band position $E_{(\pi,0)}$ agrees with that of T_χ, below which $\chi(T)$ decreases from the maximum value, if the relationship for the d-wave mean-field relation $E_{(\pi,0)} = 4.3\ k_BT/2$ is assumed. Figure 9(a) shows angle-integrated spectra obtained by integrating ARPES spectra in the second BZ, where

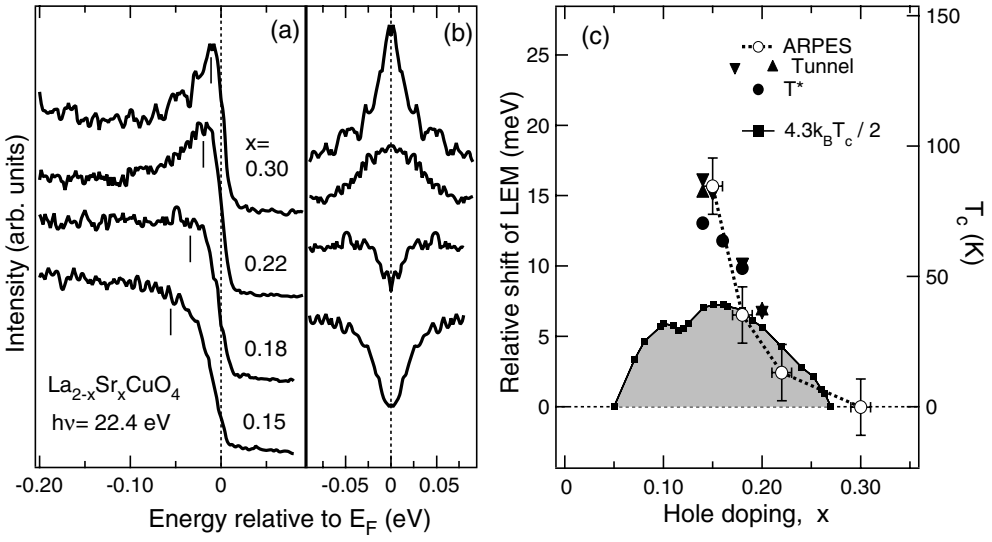

Figure 10. ARPES spectra on the Fermi surface in the antinodal region. (a) EDC for each doping. (b) Symmetrized spectra of (a). (c) Relative shift of the leading-edge midpoint (LEM) in the ARPES spectra in (a). The LEM shift is compared with the T_c (filled square) and the gap measured by scanning tunnel spectroscopy (filled triangles) [53], assuming the relationship $E = 4.3\ k_B T$ between energy and temperature [54].

$E_{(\pi,0)}$ is indicated by vertical bars. Since the flat band gives a singularity in the density of states (DOS), the corresponding maximum is seen at $E_{(\pi,0)}$ in the angle-integrated spectra [51, 52]. This energy scale may be related to the strong suppression of the spectral weight over an extended energy range, particularly prominent near $(\pi, 0)$. These results are consistent with the theoretical prediction of ETT that $E_{(\pi,0)}$ is a crucial factor to determine the quantum critical point [39].

Next, we discuss the relationship between the small pseudogap behaviours of the thermodynamic and transport properties and the low-energy spectral feature of ARPES spectra. Figure 10(a) shows ARPES spectra on the Fermi surface in the antinodal direction. In order to clearly show the gap opening, the spectra in figure 10(a) have been symmetrized with respect to E_F as shown in figure 10(b). For $x = 0.3$ and 0.22, the symmetrized spectra show a peak at the chemical potential, in contrast to those for $x = 0.15$, corresponding to the normal Fermi-liquid behaviour of the transport results [31]. Figure 10(c) shows the doping dependence of the relative energy of the leading edge midpoint (LEM). Although the LEM in $x = 0.22$ is above the Fermi level in spite of $T_c > 10$ K, it is below that of the non-superconducting sample $x = 0.3$ by ∼(2–3) meV, implying the existence of a small gap. Note that, when the QP is at the Fermi level, the LEM would be above the Fermi level due to the energy broadening under the finite energy resolution. As seen in figure 10(c), the observed gap corresponds well to the small pseudogap observed by the scanning tunnelling measurements.

4. Effects of electron–phonon coupling

It has been recognized from the very beginning of the high-T_c research that many-body effects are key to understanding cuprate physics. Due to its proximity to the antiferromagnetic Mott insulating state, electron–electron interactions are extensively discussed in the literature [1, 55].

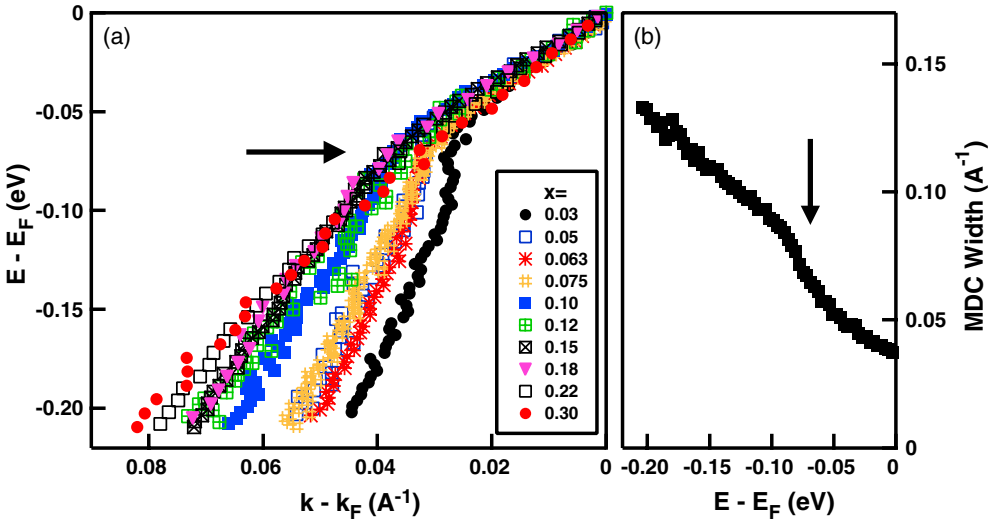

Figure 11. Doping dependence of the nodal QP in LSCO [43]. (a) Dispersion of LSCO with various doping levels ($x = 0.03$–0.30) measured at 20 K along the (0, 0)–(π, π) nodal direction. (b) Scattering rate as measured by MDC width (full width at half maximum, FWHM) of the LSCO ($x = 0.063$) sample measured at 20 K.

In this section, we shall briefly describe the present status of our understanding of electrons interacting with phonons. A more comprehensive review is presented elsewhere [56].

4.1. Electron–phonon coupling along the nodal direction

The d-wave superconducting gap is zero along the nodal direction. As shown in figure 11(a), the energy–momentum dispersion curves from the MDC method exhibit an abrupt slope change ('kink') near 70 meV. The kink is accompanied by an accelerated drop in the MDC width at a similar energy scale (figure 11(b)). The existence of the kink has been well established as ubiquitous in hole-doped cuprate materials [57, 42, 58–60, 43, 61]:

(i) It is present in various hole-doped cuprate materials, including Bi2212, $Bi_2Sr_2CuO_6$ (Bi2201), LSCO and others. The energy scale (in the range of 50–70 meV) at which the kink occurs is similar for various systems.
(ii) It is present both below T_c and above T_c.
(iii) It is present over the entire doping range (figure 11(a)). The kink effect is stronger in the underdoped region and gets weaker with increasing doping.

While there is a consensus on the data, the exact meaning of the data is still under discussion. The first issue concerns whether the kink in the normal state is related to an energy scale. Valla *et al* [62] argued that the system is quantum critical and thus has no energy scale, even though a band renormalization is present in the data. Since their data do not show a sudden change in the scattering rate at the corresponding energy, they attributed the kink in Bi2212 above T_c to the marginal Fermi liquid (MFL) behaviour without an energy scale [59]. Others believe the existence of energy scale in the normal and superconducting states has a common origin, i.e. coupling of quasiparticles with low-energy collective excitations (bosons) [57, 42, 58]. The sharp kink structure in dispersion and concomitant existence of a drop in the scattering rate, which is becoming increasingly clear with the improvement of

signal to noise in the data, as exemplified in underdoped LSCO ($x = 0.063$) in the normal state (figure 11(b)) [43], are apparently hard to reconcile with the MFL behaviour.

A further issue concerns the origin of the bosons involved in the coupling, with a magnetic resonance mode [58, 59] and optical phonons [42] being possible candidates considered. The phonon interpretation is based on the fact that the sudden band renormalization (or 'kink') effect is seen for different cuprate materials, at different temperatures, and at a similar energy scale over the entire doping range [42]. For the nodal kink, the phonon considered in the early work was the half-breathing mode, which shows an anomaly in neutron experiments [63, 64]. Unlike the phonons, which are similar in all cuprates, the magnetic resonance (at correct energy) is observed only in certain materials and only below T_c. The absence of the magnetic mode in LSCO and the appearance of the magnetic mode only below T_c in some cuprate materials are not consistent with its being the cause of the universal presence of the kink effect. Whether the magnetic resonance can cause any additional effect is still an active research topic [65, 66].

While the nodal data clearly reveal the presence of coupling to collective modes with well defined energy scale, there are a couple of peculiar behaviours associated with the doping evolution of the nodal dispersion. As seen from figure 11(a), the low-energy dispersion and velocity from the MDC method is insensitive to doping over the entire doping range, while the high energy velocity increases with decreasing doping [43]. In terms of conventional electron–phonon coupling, if one considers that the 'bare band' does not change with doping but the electron–phonon coupling strength increases with decreasing doping, as is probably the case for LSCO, one would expect that the low-energy dispersion and velocity show strong doping dependence, while the high-energy ones converge. This is opposite to the experimental observations. Moreover, considering the electron–electron interaction gets stronger with decreasing doping, according to conventional wisdom, this would result in a larger effective mass and smaller velocity, which is again opposite to experimental observation (figure 11(a)). These anomalies indicate a potential deviation from the standard Migdal–Eliashberg theory and the possibility of a complex interplay between electron–electron and electron–phonon interactions. This phenomenon is a hint of the polaronic effect where the traditional analysis fails. Such a polaron effect gets stronger in a deeply underdoped system even along the nodal direction. It is noted that, while the low-energy velocity is rather 'universal' via MDC analysis, the low-energy dispersions derived from EDC and MDC methods are rather different [19]. The difference is most pronounced at low doping, where the coupling is strong. In this case, the EDC-derived velocity exhibits considerable doping dependence. While for weakly interacting systems MDC and EDC are expected to yield similar dispersion relations from linearly dispersing bands, strong-coupling features which cause substantial renormalizations may cloud EDC and MDC analysis. The origin of the difference between MDC and EDC-derived dispersions remains a matter to be further explored.

4.2. Multiple modes in the electron self-energy

In conventional superconductors, the successful extraction of the phonon spectral function, or the Eliashberg function, $\alpha^2 F(\omega)$, from electron tunnelling data played a decisive role in cementing the consensus on the phonon-mediated mechanism of superconductivity [67]. For high-temperature superconductors, the extraction of the bosonic spectral function can provide fingerprints for more definitive identification of the nature of bosons involved in the coupling.

In principle, the ability to directly measure the dispersion, and therefore the electron self-energy, would make ARPES the most direct way of extracting the bosonic spectral function. This is because, in metals, the real part of the electron self-energy $\mathrm{Re}\Sigma$ is related to the

Eliashberg function $\alpha^2 F(\Omega; \epsilon, \hat{\mathbf{k}})$ by

$$\mathrm{Re}\,\Sigma(\hat{\mathbf{k}}, \epsilon; T) = \int_0^\infty \mathrm{d}\Omega\, \alpha^2 F(\Omega; \epsilon, \hat{\mathbf{k}}) K\left(\frac{\epsilon}{kT}, \frac{\hbar\Omega}{kT}\right), \tag{2}$$

where

$$K(y, z) = \int_{-\infty}^{\infty} \mathrm{d}x \frac{2z}{x^2 - z^2} f(x + y), \tag{3}$$

with $f(x)$ being the Fermi distribution function. Such a relation can be extended to any electron–boson coupling system and the function $\alpha^2 F(\omega)$ then describes the underlying bosonic spectral function. Unfortunately, given that the experimental data inevitably have noise, the traditional least-squares method to invert an integral problem is mathematically unstable.

Very recently, Shi *et al* have made an important advance in extracting the Eliashberg function from ARPES data by employing the maximum entropy method (MEM) and successfully applied the method to Be surface states [68]. The MEM approach [68] is advantageous over the least-squares method in that (i) it treats the bosonic spectral function to be extracted as a probability function and tries to obtain the most probable one; (ii) more importantly, it is a natural way to incorporate the *priori* knowledge as a constraint into the fitting process. In practice, to achieve an unbiased interpretation of data, only a few basic physical constraints to the bosonic spectral function are imposed. (A) It is positive. (B) It vanishes at the limit $\omega \to 0$. (C) It vanishes above the maximum energy of the self-energy features. As shown in the case of the Be surface state, this method is robust in extracting the Eliashberg function [68].

Initial efforts have been made to extend this approach to underdoped LSCO and evidence for electron coupling to several phonon modes has been revealed [69]. As seen from figure 12, from both the electron self-energy (figure 12(a)), and the derivative of their fitted curves ((figure 12(a)), one can identify two dominant features near ∼40 and ∼60 meV. In addition, two addition modes may also be present near ∼25 and ∼75 meV [69]. The multiple features in figure 12(b) show marked differences from the magnetic excitation spectra measured in LSCO, which is mostly featureless and doping dependent [70]. In comparison, they show more resemblance to the phonon density of states (DOS), measured from neutron scattering on LSCO (figure 12(c)) [71], in the sense of the number of modes and their positions. This similarity between the extracted fine structure and the measured phonon features favours phonons as the bosons coupling to the electrons. In this case, in addition to the half-breathing mode at 70–80 meV that we previously considered strongly coupled to electrons [42], the present results suggest that several lower-energy optical phonons of oxygens are also actively involved.

We note that, in order to be able to identify fine structure in the electron self-energy, it is imperative to have both high energy resolution and high statistics [72]. These requirements have made the experiment highly challenging because of the necessity to compromise between two conflicting requirements for the synchrotron light source: high energy resolution and high photon flux. Further improvements in photoemission experiments will probably enable a detailed understanding of the boson modes coupled to electrons, and provide critical information for the pairing mechanism.

5. Relation to thermodynamic and transport properties

The thermodynamic and transport properties of the high-T_c cuprates are fundamentally affected by the strong electron correlation near the filling-control Mott transition, particularly by the opening of the pseudogap as implied by figure 1. The electronic specific heat coefficient γ decreases with decreasing hole concentration in the underdoped region [9]. The

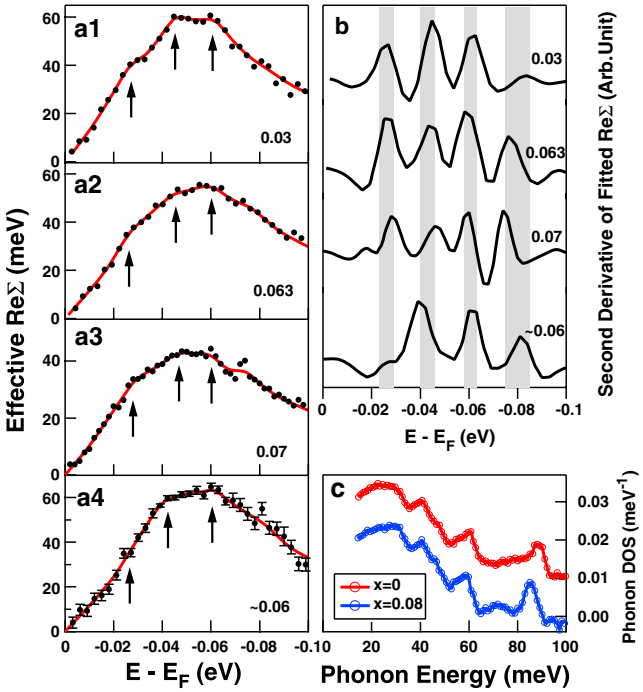

Figure 12. Multiple modes coupling in the electron self-energy in LSCO [69]. (a) Effective real part of the electron self-energy for LSCO $x = 0.03$ (a1), 0.063 (a2), 0.07 (a3) and ∼0.06 (a4) samples. (b). Second-order derivative of the calculated Re Σ. The four shaded areas correspond to energies of 23–29, 40–46, 58–63 and 75–85 meV where the fine features fall. (c) Phonon density of states $F(\omega)$ for LSCO $x = 0$ (upper) and $x = 0.08$ (lower) measured by neutron scattering [71].

electrical resistivity shows unconventional electrical resistivity such as the T-linear temperature dependence in the optimally doped region [31] and the metallic behaviour with resistivity well exceeding the Ioffe–Regel limit in the lightly doped region [37]. In order to elucidate the origin of these unconventional phenomena, in this section, we shall attempt to explain the doping dependence of the electronic specific heat coefficient γ, the superfluid density, the electrical resistivity and the Hall coefficient on the basis of the ARPES results.

5.1. Electronic specific heat

The electronic specific heat coefficient γ of a Fermi liquid is given by $\gamma = (\pi^2 k_B^2/3)N(0)^*$, where $N(0)^*$ is the QP density of states (DOS) at the chemical potential. In a single-band system like single-layer cuprates, each momentum $\mathbf{k}$ contributes one QP, if the system is a Fermi liquid. Therefore, by using the Fermi velocity v_F of the QP band along the Fermi surface, one can deduce the two-dimensional QP DOS $N(0)^*$ using the formula $N(0)^* = (1/2\pi^2)\int ds/\hbar v_F$, where the integration is made over the Fermi surface.

In order to take into account the effect of the pseudogap in the present analysis, we first attempted to derive the length of the Fermi arc. From symmetrized EDCs on the (underlying) Fermi surface as shown in figures 13(a)–(c), we have defined the arc length by the portion of the (underlying) Fermi surface showing a single QP peak at the chemical potential. As shown in figure 13(d), one can see that the arc length evolves with hole doping systematically and eventually it becomes a fully extended (100%) closed Fermi surface in overdoped $x = 0.22$.

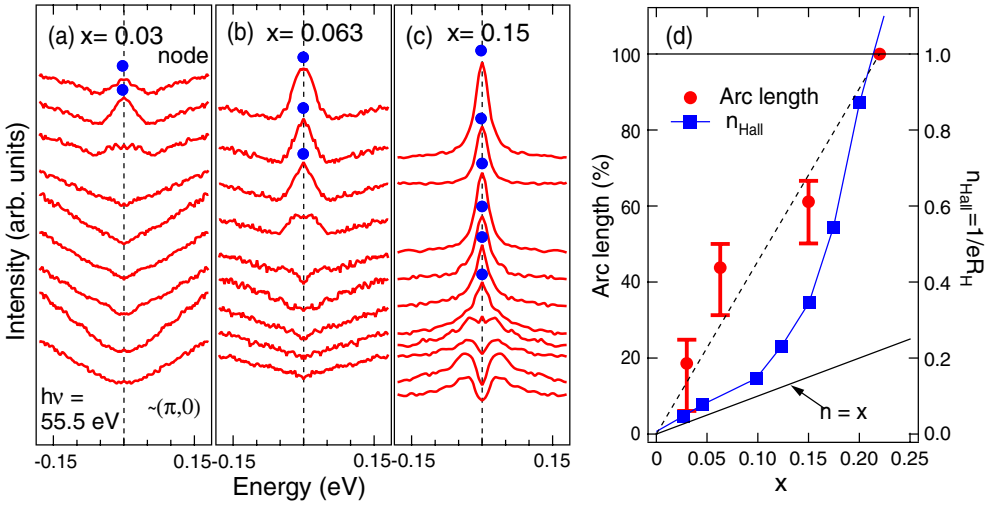

Figure 13. Symmetrized EDCs along the (underlying) Fermi surface for $x = 0.03$ (a), $x = 0.063$ (b) and $x = 0.15$ (c). Panel (d) shows the arc length ratio defined by the fraction of the Fermi surface length which shows a QP peak as in the symmetrized EDCs. Curves for $n = x$ and $n_{\mathrm{Hall}} = 1/eR_{\mathrm{H}}$ [31] are also shown.

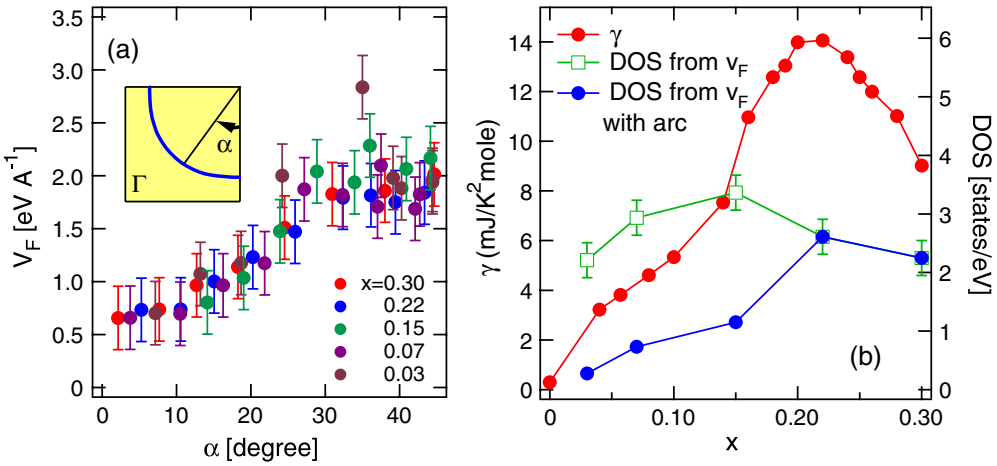

Figure 14. Density of states at the chemical potential in LSCO. (a) Fermi velocity v_{F} along the Fermi surface. (b) Comparison of the electronic specific heat coefficient γ [9] and the QP DOS at the chemical potential calculated using v_{F} from ARPES data. The QP DOS from ARPES with the arc length taken into account is also shown.

The carrier number defined by $n_{\mathrm{Hall}} = 1/eR_{\mathrm{H}}$ are compared with the arc length in figure 13(d). The difference between n_{Hall} and the arc length may come from the fact that n_{Hall} is affected by the curvature of the Fermi surface, too [73]. Note, however, that due to the finite energy resolution, two closely spaced QP peaks may not be resolved in the symmetrized EDCs and the arc length may be overestimated.

Figure 14(a) shows the Fermi velocity v_{F} for various doping levels determined from the observed QP dispersions as a function of Fermi-surface angle α. Here, we have used MDC for determining v_{F} in a similar manner as in figure 11, while an alternative way is to use EDCs [74].

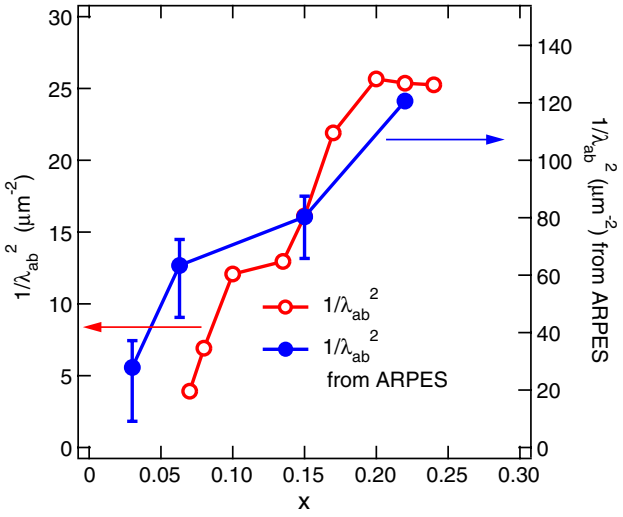

Figure 15. In-plane superfluid density deduced from the magnetic penetration depth λ_{ab} [76] compared with that estimated from the ARPES data.

One can see that the v_F remains relatively unchanged with hole doping not only in the node direction ($\alpha = 45°$; see figure 11) but also on the entire Fermi surface. In figure 14(b), the electronic specific heat coefficient γ calculated using the v_F values thus deduced is compared with the γ of LSCO samples where the T_c was suppressed by Zn doping [9]. The $N(0)^*$ calculated from ARPES has a maximum around $x = 0.15$ because the flat band near $(\pi, 0)$ becomes closest to the Fermi level. If the system is a Fermi liquid, $N(0)^*$ from ARPES and γ should agree with each other. However, γ decreases much faster than $N(0)^*$ from ARPES with decreasing x, indicating that the QP density at the chemical potential is indeed depleted in the underdoped materials and demonstrating that the opening of the pseudogap around $(\pi, 0)$ affects the low-energy QP excitations. If the shrinking arc length is taken into account, one can qualitatively reproduce the decrease of γ with decreasing x. As for the absolute values, however, the experimental values are larger than those deduced from ARPES by a factor of $\sim$2. The origin of this discrepancy is not known at present.

5.2. Superfluid density

Comparison between the ARPES spectra and the superfluid density would also give important information about the pseudogap opening and its effects on the superconductivity [75]. The in-plane London penetration depth λ_{ab} and the superfluid density $\rho_s = n_s/m^*$ are related through $1/\lambda_{ab}^2 = \mu_0 e^2 n_s/m^*$, where μ_0 is the vacuum permeability, and n_s is the density of superconducting electrons. For the density of superconducting electrons, we assumed that n_s per Cu atom is given by $(1-x)\times$ (arc length), where the doping dependence of the arc length is given in figure 13(d). Since the nodal direction rather than the antinodal direction is expected to be the main contribution to the in-plane superfluid density due to the lighter effective mass, m^* was approximated by $m^* = \hbar k_F/v_F$, where v_F is the Fermi velocity in the nodal direction [43] (section 4.1). In figure 15, the doping dependence of $1/\lambda_{ab}^2$ [76] is compared with that deduced from the ARPES data. The two curves show qualitatively good agreement between them. Considering that m^* is nearly independent of doping [43], the doping dependence of the arc length is the principal origin of the doping dependence of n_s. Quantitatively, however, the $1/\lambda_{ab}^2$

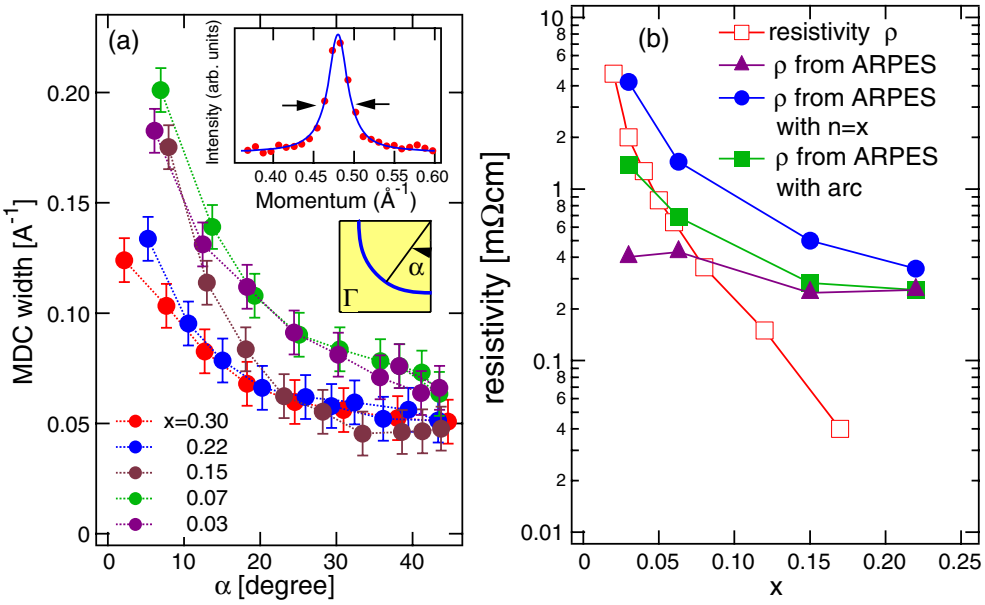

Figure 16. Electrical resistivity of LSCO estimated from ARPES. (a) MDC width for various doping levels plotted as a function of Fermi-surface angle α. (b) Comparison of the resistivity estimated using the MDC width and the electrical resistivity at 20 K [37]. For the transport data for those compositions which show localization behaviour at low temperatures, the minimum resistivity at a higher temperature is adopted.

values show a difference of factor ∼5, implying that the effective density of superconducting electrons is reduced compared with the nominal carrier number even in the overdoped region. Also, note that the superfluid density becomes finite only for $x > 0.05$, while that estimated from ARPES shows finite value even for $x = 0.03$. Another viewpoint to explain the reduced superfluid density is to attribute it to the reduced QP spectral weight Z rather than the enhanced m^* [75, 77], which also explains the doping dependence of $1/\lambda_{ab}^2$ (see figure 3(c)). The overall quantitative difference may come from the effect of Z.

5.3. Electrical resistivity

Because of the pseudo-gap opening around $(\pi, 0)$, the electronic states around the node mainly contribute to the in-plane transport properties in the underdoped region. Here, we have attempted to estimate the in-plane electrical resistivity from the observed MDC width $\Delta k = 1/l_k$ (figure 16(a)), where l_k is the mean free path, and the length of the 'Fermi arc' obtained in section 5.1 as follows. In the simple Drude formula, the resistivity is given by $\rho = m^*/ne^2\tau = \hbar k_F \Delta k/ne^2$. It is often assumed that $n = x$ based on the Hall coefficient results [31]. In the Boltzmann equation in two dimensions, the diagonal component of the conductivity is given by $\sigma_{xx} = (e^2/h\pi)\int l_k \cos^2\theta_k \, ds$, where the integration is made over the Fermi surface, and θ_k is the angle between $\mathbf{l}_k = \mathbf{v}_F\tau_k$ and the electric field taken parallel to the x-axis [73]. Using ARPES data of high-T_c cuprates, the electrical resistivity at high temperatures, where the pseudogap disappears, has been calculated using this method [78]. In addition to this treatment, we have taken into account the effect of 'Fermi arc' by reducing the integration length on the Fermi surface.

The MDC width at the chemical potential is plotted in figure 16(a) as a function of Fermi-surface angle α. One can see that the width around the node ($\alpha = 45°$) depends on doping only weakly, which is consistent with the weak doping dependence of the charge mobility $\mu = e\tau/m^* = e/\hbar k_F \Delta k$ [37]. Using the data in figure 16(a), the doping dependence of the in-plane electrical resistivity ρ was estimated by applying the Drude formula with $n = x$ and the nodal MDC width, and the Boltzmann formula with and without the Fermi arc. Then, they are compared with the transport results [37] in figure 16(b).

In all the ρ estimated from ARPES, the discrepancy from the transport data is pronounced in the overdoped region. The discrepancy stems from the wide MDC widths compared to that expected from the transport results in the overdoped region, which may be due to the effects of vertex correction, the possible dominance of forward scattering [79] in the overdoped region and/or the finite instrumental resolution neglected in the present analysis. On the other hand, in the underdoped region, the ρ estimated from ARPES including the effects of the 'Fermi arc' or assuming $n = x$ is in good agreement with the transport results, while that evaluated using the entire Fermi surface is smaller than the transport data by more than one order of magnitude. This suggests that the pseudogap is the origin of the small carrier number and hence the high electrical resistivity of the underdoped samples. As a whole, the ρ values estimated from ARPES with the Fermi arc explain well the doping dependence of the transport data of the underdoped LSCO.

5.4. Incommensurability in neutron scattering data

Incommensurate peaks seen in the neutron scattering experiments of LSCO [16] have been discussed as a signature of the spin-charge fluctuations in a stripe form [14, 15]. There have been several attempts to explain the incommensurability from the shape of the Fermi surface [80–82]. Recently, the QP interference has been observed in the scanning tunnelling microscopy (STM) study of Bi2212 [83, 84]. In another STM study, the observed features were discussed in connection with the stripe feature [85]. The QP interference has been explained by the autocorrelations of the ARPES intensity map in momentum space [86, 87].

Therefore, we applied the autocorrelation analysis to the present ARPES results of LSCO and found that neutron scattering peak intensity $\mathrm{Im}\,\chi_0(q, \omega = 0)$ can be approximately expressed by the autocorrelation formula $\mathrm{Im}\,\chi_0(q, 0) \sim \Sigma_k A(k, 0)A(k + q, 0)$ as shown in figure 17. Although this formula may not be sufficient for correlated electron systems, autocorrelation analysis may give some insight into the problem of the incommensurability. Figure 17(b) shows that the obtained incommensurability increases with hole doping, although there are quantitative deviations from the neutron results. Also, it should be noted that neutron scattering for $x = 0.03$ shows diagonal peaks, whereas our incommensurate peaks remained vertical. In the present autocorrelation model, such an increase of the incommensurability can be attributed to the decreasing Fermi momentum k_F measured from the Γ point with hole doping (figure 8(b)), since the incommensurability is given by the momentum vector connecting nearly parallel part of the Fermi surface around the node, as shown in figure 17(c). The antinodal region does not contribute to the autocorrelation function because spectral weight in that region is very small due to the pseudogap opening. It is interesting to note that the $4a \times 4a$ ordering observed in Na-CCOC [88] may be related to the nesting vector $q = \pi/2a$ connecting the Fermi surface near $(\pi, 0)$ [48]. The calculated peak widths are broadened in the overdoped $x = 0.22$, which is also consistent with the neutron results. The present analysis suggests that the shape of the Fermi surface of LSCO with small $-t'/t$ may have a nesting instability of the observed incommensurability. On the quantitative level, however, the obtained incommensurability is a little different from the stripe picture,

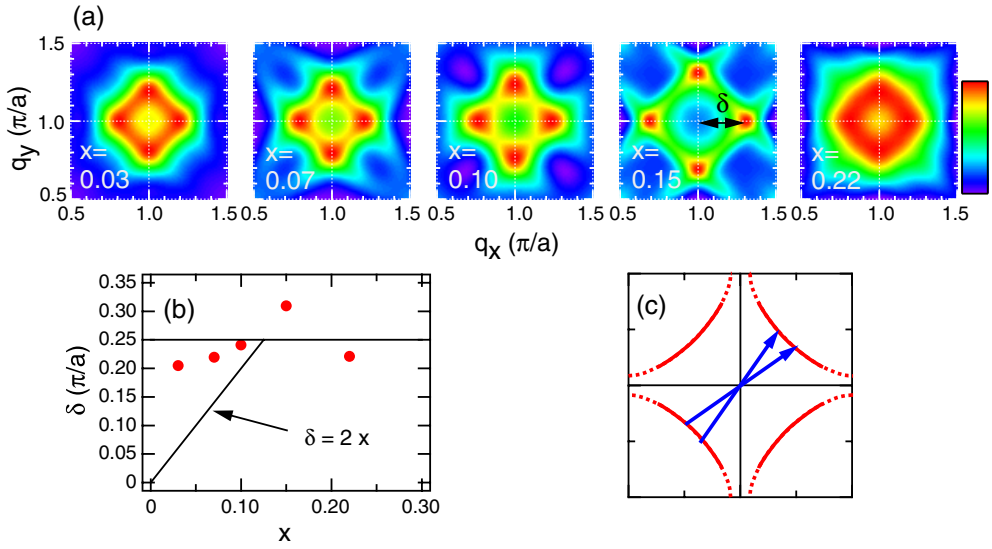

Figure 17. Autocorrelation mapping of the ARPES data for LSCO. (a) Intensity plots of $\Sigma_k A(k,0)A(k+q,0)$ for various dopings. (b) Doping dependence of the incommensurability δ obtained from the autocorrelation mapping. (c) Momentum vectors corresponding to the incommensurate peaks for $x = 0.15$.

and therefore further analysis with more sophisticated models will be needed to address the stripe issue.

6. Conclusion

We have performed a systematic ARPES study of the high-T_c cuprate LSCO from the undoped insulator to the overdoped metal. The doping dependence of the (underlying) Fermi surfaces, the QP band dispersion and the pseudogap behaviours were studied in detail. We observed a doping dependence of the TB parameter $-t'/t$, which is consistent with the LDA calculation, which takes into account the effect of apical oxygen, as well as with the CDMFT calculation, which takes into account the increased electron correlation with decreasing hole concentration. Also, the Fermi surface deduced using MDCs was found to approximately fulfil Luttinger's sum rule even down to the lightly doped region [27].

As for the QP spectral feature, in the underdoped region, apparent two-component behaviours occur with the chemical potential pinning [49]. The Fermi velocity was nearly doping independent [43] and the spectral weight of the nodal QP increased with hole doping. The length of the Fermi arc increased with hole doping. The relationship between the large pseudogap and the singularity in the DOS caused by the flat band feature is discussed. The small pseudogap observed around $(\pi, 0)$ was found to be consistent with other experimental data.

Finally, by using the information from the ARPES results, we have successfully reproduced the qualitative behaviour of the thermodynamic and transport properties of LSCO. In the analysis, we demonstrated that the pseudogap and the Fermi arc feature observed by ARPES can explain the unconventional doping dependence of the thermodynamic and transport properties of LSCO.

Although the analysis using the ARPES data can qualitatively explain many physical properties of the underdoped LSCO, quantitative discrepancies remain to be explained.

Obviously the definition of the Fermi arc and its length is rather loose and only approximate at the present stage, and will have to be further examined on a firm ground. Also, the origin of the difference between LSCO and other cuprate families such as Na-CCOC remains to be understood. The effect of different electron–phonon coupling strengths and the effect of apical oxygen leading to the different t'/t and t''/t values have to be investigated in future studies.

Acknowledgments

We are grateful to P Prelovsek, N Nagaosa, A S Mishchenko, H Fukuyama, Y Yanase, M Ogata, O K Andersen, I Dasgupta, G Kotliar, D N Basov, C M Ho, T K Lee, A Bansil, M Randeria and M Ido for enlightening discussions. This work was supported by a Grant-in-Aid for Scientific Research in Priority Area 'Invention of anomalous quantum materials', a Grant-in-Aid for Young Scientists from the Ministry of Education, Science, Culture, Sports and Technology, a US–Japan Joint Research Program from JSPS, and the USDOE. Experimental data were recorded at ALS and SSRL, which are operated by the Department of Energy's Office of Basic Energy Science.

References

[1] Damascelli A, Hussain Z and Shen Z-X 2003 *Rev. Mod. Phys.* **75** 473
[2] Feng D L *et al* 2001 *Phys. Rev. Lett.* **86** 5550
[3] Nakano T, Oda M, Manabe C, Momono N, Miura Y and Ido M 1994 *Phys. Rev.* B **49** 16000
[4] Hwang H Y, Batlogg B, Takagi H, Kao H L, Cava R J, Krajewski J J and Peck W F Jr 1994 *Phys. Rev. Lett.* **72** 2636
[5] Nishikawa T, Takeda J and Sato M 1994 *J. Phys. Soc. Japan* **63** 1441
[6] Takagi H, Batlogg B, Kao H L, Kwo J, Cava R J, Krajewski J J and Peck W F Jr 1992 *Phys. Rev. Lett.* **69** 2975
[7] Loram J W, Mirza K A, Wade J M, Cooper J R and Liang W Y 1994 *Physica* C **235** 134
[8] Nishikawa T, Shamoto S, Sera M, Sato M, Ohsugi S, Kitaoka Y and Asayama K 1993 *Physica* C **209** 553
[9] Momono N, Ido M, Nakano T, Oda M, Okajima Y and Yamaya K 1994 *Physica* C **233** 395
[10] Ino A, Kim C, Mizokawa T, Shen Z-X, Fujimori A, Takaba M, Tamasaku K, Eisaki H and Uchida S 1999 *J. Phys. Soc. Japan* **68** 1496
[11] Ino A, Kim C, Nakamura M, Yoshida T, Mizokawa T, Shen Z-X, Fujimori A, Kakeshita T, Eisaki H and Uchida S 2000 *Phys. Rev.* B **62** 4137
[12] Ino A, Kim C, Nakamura M, Yoshida T, Mizokawa T, Shen Z-X, Fujimori A, Kakeshita T, Eisaki H and Uchida S 2002 *Phys. Rev.* B **65** 094504
[13] Zhou X J *et al* 2001 *Phys. Rev. Lett.* **86** 5578
[14] Zaanen J and Oleś A M 1996 *Ann. Phys., Lpz.* **5** 224
[15] Salkola M I, Emery V J and Kivelson S A 1996 *Phys. Rev. Lett.* **77** 155
[16] Tranquada J M, Sternlieb B J, Axe J D, Nakamura Y and Uchida S 1995 *Nature* **375** 561
[17] Shen K M *et al* 2004 *Phys. Rev. Lett.* **93** 267002
[18] Rösch O, Gunnarsson O, Zhou X J, Yoshida T, Sasagawa T, Fujimori A, Hussain Z, Shen Z-X and Uchida S 2005 *Phys. Rev. Lett.* **95** 227002
[19] Mishchenko A S, Nagaosa N, Shen K M, Shen Z-X, Zhou X J and Devereaux T P, unpublished
[20] Bansil A and Lindroos M 1999 *Phys. Rev. Lett.* **83** 5154
[21] Tohyama T, Nagai S, Shibata Y and Maekawa S 1999 *Phys. Rev. Lett.* **82** 4910
[22] Fleck M, Lichtenstein A I, Pavarini E and Oles A M 2000 *Phys. Rev. Lett.* **84** 4962
[23] Ichioka M and Machida K 1999 *J. Phys. Soc. Japan* **68** 4020
[24] Machida K and Ichioka M 1999 *J. Phys. Soc. Japan* **68** 2168
[25] Yoshida T *et al* 2001 *Phys. Rev.* B **63** 220501
[26] Yoshida T *et al* 2003 *Phys. Rev. Lett.* **91** 027001
[27] Yoshida T *et al* 2005 *Preprint* cond-mat0510608
[28] Fukuyama H and Kohno H 1999 *Physics and Chemistry of Transition-Metal Oxides* ed H Fukuyama and N Nagaosa (Berlin: Springer) p 231
[29] Yanase Y, Jujo T, Nomura T, Ikeda H, Hotta T and Yamada K 2003 *Phys. Rep.* **387** 1

[30] Tokura Y, Taguchi Y, Okada Y, Fujishima Y, Arima T, Kumagai K and Iye Y 1993 *Phys. Rev. Lett.* **70** 2126
[31] Takagi H, Ido T, Ishibashi S, Uota M, Uchida S and Tokura Y 1989 *Phys. Rev.* B **40** 2254
[32] Uemura Y J *et al* 1991 *Phys. Rev. Lett.* **66** 2665
[33] Uchida S, Ido T, Takagi H, Arima T, Tokura Y and Tajima S 1991 *Phys. Rev.* B **43** 7942
[34] Wells B O, Shen Z-X, Matsuura A, King D M, Kastner M A, Greven M and Birgeneau R J 1995 *Phys. Rev. Lett.* **74** 964
[35] Tohyama T and Maekawa S 2000 *Supercond. Sci. Technol.* **13** R17
[36] Nazarenko A, Vos K J E, Haas S, Dagotto E and Gooding R J 1995 *Phys. Rev.* B **51** 8676
[37] Ando Y, Lavrov A N, Komiya S, Segawa K and Sun X F 2001 *Phys. Rev. Lett.* **87** 017001
[38] Dumm M, Komiya S, Ando Y and Basov D N 2003 *Phys. Rev. Lett.* **91** 077004
[39] Onufrieva F and Pfeuty P 2000 *Phys. Rev.* B **61** 799
[40] Mayr M, Alvarez G, Moreo A and Dagotto E 2006 *Phys. Rev.* B **73** 014509
[41] Capone M, Sangiovanni G, Castellani C, Castro C D and Grilli M 2004 *Phys. Rev. Lett.* **92** 106401
[42] Lanzara A *et al* 2001 *Nature* **412** 510
[43] Zhou X J *et al* 2003 *Nature* **423** 398
[44] Sahrakorpi S, Lindroos M, Markiewicz R S and Bansil A 2005 *Phys. Rev. Lett.* **95** 157601
[45] Radaelli P G, Hinks D G, Mitchell A W, Hunter B A, Wagner J L, Dabrowski B, Vandervoort K G, Viswanathan H K and Jorgensen J D 1994 *Phys. Rev.* B **49** 4163
[46] Pavarini E, Dasgupta I, Saha-Dasgupta T, Jepsen O and Andersen O K 2001 *Phys. Rev. Lett.* **87** 047003
[47] Civelli M, Capone M, Kancharla S S, Parcollet O and Kotliar G 2005 *Phys. Rev. Lett.* **95** 106402
[48] Kyle M *et al* 2005 *Science* **307** 901
[49] Ino A, Mizokawa T, Fujimori A, Tamasaku K, Eisaki H, Uchida S, Kimura T, Sasagawa T and Kishio K 1997 *Phys. Rev. Lett.* **79** 2101
[50] Yagi H, Yoshida T, Fujimori A, Kohsaka Y, Misawa M, Sasagawa T, Takagi H, Azuma M and Takano M 2006 *Phys. Rev.* B **73** 172503
[51] Ino A, Mizokawa T, Kobayashi K, Fujimori A, Sasagawa T, Kimura T, Kishio K, Tamasaku K, Eisaki H and Uchida S 1998 *Phys. Rev. Lett.* **81** 2124
[52] Sato T, Yokoya T, Naitoh Y, Takahashi T, Yamada K and Endoh Y 1999 *Phys. Rev. Lett.* **83** 2254
[53] Nakano T, Momono N, Oda M and Ido M 1998 *J. Phys. Soc. Japan* **67** 2622
[54] Won H and Maki K 1994 *Phys. Rev.* B **49** 1397
[55] Campuzano J C, Norma M R and Randeria M 2004 *Physics of Superconductors* vol 2, ed K H Bennemann and J B Ketterson (Berlin: Springer) pp 167–273
[56] Zhou X J, Cuk T, Devereaux T, Nagaosa N and Shen Z-X 2006 *Treatise of High Temperature Superconductivity* ed J Robert Schrieffer at press
(Zhou X J, Cuk T, Devereaux T, Nagaosa N and Shen Z-X 2006 *Preprint* cond-mat/0604284)
[57] Bogdanov P V *et al* 2000 *Phys. Rev. Lett.* **85** 2581
[58] Eschrig M and Norman M R 2000 *Phys. Rev. Lett.* **85** 3261
[59] Johnson P D *et al* 2001 *Phys. Rev. Lett.* **87** 177007
[60] Borisenko S V, Kordyuk A A, Kim T K, Koitzsch A, Knupfer M, Fink J, Golden M S, Eschrig M, Berger H and Follath R 2003 *Phys. Rev. Lett.* **90** 207001
[61] Gweon G-H, Sasagawa T, Zhou S Y, Graf J, Takagi H, Lee D-H and Lanzara A 2004 *Nature* **430** 187
[62] Valla T, Fedorov A V, Johnson P D, Wells B O, Hulbert S L, Li Q, Gu G D and Koshizuka N 1999 *Science* **285** 2110
[63] Pintschovius L and Braden M 1999 *Phys. Rev.* B **60** R15039
[64] McQueeney R J, Petrov Y, Egami T, Yethiraj M, Shirane G and Endoh Y 1999 *Phys. Rev. Lett.* **82** 628
[65] Kee H-Y, Kivelson S and Aeppli G 2002 *Phys. Rev. Lett.* **88** 257002
[66] Ar Abanov, Chubukov A V, Eschrig M, Norman M R and Schmalian J 2002 *Phys. Rev. Lett.* **89** 177002
[67] Rowell J M, Anderson P W and Thomas D E 1963 *Phys. Rev. Lett.* **10** 334
Scalapino D J, Schrieffer J R and Wilkins J W 1966 *Phys. Rev.* **148** 263
[68] Shi J R *et al* 2004 *Phys. Rev. Lett.* **92** 186401
[69] Zhou X J *et al* 2005 *Phys. Rev. Lett.* **95** 117001
[70] Hayden S M, Aeppli G, Mook H A, Perring T G, Mason T E, Cheong S-W and Fisk Z 1996 *Phys. Rev. Lett.* **76** 1344
Hiraka H, Endoh Y, Fujita M, Lee Y S, Kulda J, Ivanov A and Birgeneau R J 2001 *J. Phys. Soc. Japan* **70** 853
Goka H, Kuroshima S, Fujita M, Yamada K, Hiraka H, Endoh Y and Frost C D 2003 *Physica* C **388/389** 239
Tranquada J M, Woo H, Perring T G, Goka H, Gu G D, Xu G, Fujita M and Yamada K 2004 *Nature* **429** 534
[71] McQueeney R J, Sarrao J L, Pagliuso P G, Stephens P W and Osborn R 2001 *Phys. Rev. Lett.* **87** 077001
[72] Valla T 2006 *Phys. Rev. Lett.* **96** 119701

Zhou X J, Shi J, Yang W L, Komiya S, Ando Y, Plummer W, Hussain Z and Shen Z-X 2006 *Phys. Rev. Lett.* **96** 119702
[73] Ong N P 1991 *Phy. Rev.* B **43** 193
[74] Mannella N, Yang W L, Zhou X J, Zheng H, Mitchell J F, Zaanen J, Devereaux T P, Nagaosa N, Hussain Z and Shen Z-X 2005 *Nature* **438** 474
[75] Feng D L *et al* 2000 *Science* **289** 277
[76] Panagopoulos C, Xiang T, Anukool W, Cooper J R, Wang Y S and Chu C W 2003 *Phys. Rev.* B **67** 220502
[77] Paramekanti A, Randeria M and Trivedi N 2001 *Phys. Rev. Lett.* **87** 217002
[78] Kondo T, Takeuchi T, Yokoya T, Tsuda S, Shin S and Mizutani U 2005 *J. Electron Spectrosc. Relat. Phenom.* **144–147** 1249
[79] Zhu L, Hirschfeld P J and Scalapino D J 2004 *Phys. Rev.* B **70** 214503
[80] Si Q, Zha Y, Levin K and Lu J P 1993 *Phys. Rev.* B **47** 9055
[81] Kao Y, Si Q and Levin K 2000 *Phys. Rev.* B **61** R11898
[82] Kuroki K, Arita R and Aoki H 1999 *Phys. Rev.* B **60** 9850
[83] McElroy K, Simmonds R W, Hoffman J E, Lee D-H, Orenstein J, Eisaki H, Uchida S and Davis J C 2003 *Nature* **422** 592
[84] Hoffman J E, McElroy K, Lee D-H, Lang K M, Eisaki H, Uchida S and Davis J C 2002 *Science* **297** 1148
[85] Howald C, Eisaki H, Kaneko N, Greven M and Kapitulnik A 2003 *Phys. Rev.* B **67** 014533
[86] McElroy K, Lee D-H, Hoffman J E, Lang K M, Lee J, Hudson E W, Eisaki H, Uchida S and Davis J C 2005 *Phys. Rev. Lett.* **94** 197005
[87] Chatterjee U *et al* 2006 *Phys. Rev. Lett.* **96** 107006
[88] Hanaguri T, Lupien C, Kohsaka Y, Lee D-H, Azuma M, Takano M, Takagi H and Davis J C 2004 *Nature* **430** 1001